Precipitation Budget of the Madden–Julian Oscillation

ÁNGEL F. ADAMES

NOAA/Geophysical Fluid Dynamics Laboratory, Princeton University, Princeton, New Jersey

ABSTRACT

Column moisture and moist static energy (MSE) budgets have become common tools in the study of the processes responsible for the maintenance and evolution of the MJO. While many studies have shown that precipitation is spatially correlated with column moisture, these budgets do not directly describe the MJO-related precipitation anomalies. Other spatially varying fields may also play a role in determining the horizontal distribution of anomalous precipitation. In this study, an empirical precipitation anomaly field is derived that depends on three variables in addition to column moisture. These are the low-frequency distribution of precipitation, the low-frequency column saturation water vapor, and the sensitivity of precipitation to changes in column relative humidity. The addition of these fields improves upon moisture/MSE budgets by confining these anomalies to the climatologically rainy areas of the tropics, where MJO activity is strongest. The derived field adequately describes the MJO-related precipitation anomalies, comparing favorably with TRMM precipitation data.

Furthermore, a "precipitation budget" is presented that emphasizes moist processes over the regions where precipitation is most sensitive to free-tropospheric moisture. It is found that moistening from vertical moisture advection in association with regions of shallow ascent plays a central role in the propagation of the MJO. The overall contribution from this process is comparable to the contribution from horizontal moisture advection to propagation. Consistent with previous studies, it is found that vertical advection arising from longwave radiative heating maintains the intraseasonal precipitation anomalies against drying by horizontal moisture advection.

1. Introduction

The Madden–Julian oscillation (Madden and Julian 1971, 1972) is one of the most prominent features of the tropical atmosphere at the intraseasonal (30–90 day) time scale (Zhang 2005; Lau and Waliser 2011). It is characterized by an envelope of enhanced and suppressed convection several thousand kilometers across, coupled to planetary-scale features that resemble the Matsuno–Gill (Matsuno 1966; Gill 1980) response to an equatorial heat source. This large-scale coupling between circulation and convection propagates eastward at $\sim 5\,\mathrm{m\,s}^{-1}$, with widespread influences on weather patterns across the globe [Zhang (2013) and references therein]. In spite of increased international effort to improve our understanding of the MJO (Waliser et al. 2009; Yoneyama et al. 2013; Zhang et al. 2013), the mechanisms in which large-scale convection is maintained and propagates eastward are not entirely understood.

In spite of the many challenges facing our understanding of the MJO, several key features have been identified. Among these is the importance of the three-way interaction between moisture, convection, and radiation in the maintenance of the precipitation anomalies (Raymond 2001; Kim et al. 2015; Del Genio et al. 2015). Furthermore, recent studies have suggested that the eastward propagation of the anomalous precipitation in the MJO is predominantly driven by two mechanisms. One is horizontal advection of moisture driven by the MJO's anomalous lower-tropospheric wind field (Maloney 2009; Zhao et al. 2013; Pritchard and Bretherton 2014; Kim et al. 2014a; Zhu and Hendon 2015; among others). The other mechanism is free-tropospheric moistening arising from vertical motion, either by cloud-related moisture fluxes (Benedict and Randall 2007; Hannah et al. 2016; Powell and Houze 2015; Powell 2016) or forced by equatorial wave motion (Wang 1988; Hsu and Li 2012; Liu and Wang 2016). The importance of coupling

Corresponding author e-mail: Ángel F. Adames, angel. adames-corraliza@noaa.gov

between moisture and convection in MJO dynamics has led many authors to conclude that the MJO is the result of a modal instability that results from moisture–convection–radiation feedbacks, often referred to as "moisture mode" instability (Raymond and Fuchs 2009; Sugiyama 2009; Sobel and Maloney 2012, 2013).

Recently, Adames and Kim (2016), expanded upon the moisture-mode theoretical framework. Their modifications led to a dispersion relation where the wind anomalies in the Matsuno–Gill response advect mean moisture such that the rainbands propagate eastward while wave activity propagates westward. Their dispersion relation suggests that the maintenance and propagation of the MJO depends on a parameter that characterizes the sensitivity of precipitation to changes in column water vapor, known as the convective adjustment time scale τ_c (Bretherton et al. 2004). The relationship between this parameter and the MJO and how it varies in space has not been thoroughly investigated.

In this study, we will show that the evolution of the MJO's precipitation features is not only dependent on anomalous column water vapor but also on the climatological-mean distribution of precipitation, which determines the aforementioned convective adjustment time scale. By incorporating this convective adjustment time scale onto the moisture field, an estimate of the intraseasonal precipitation anomalies is obtained that compares favorably with observations. Moreover, a prognostic equation for precipitation is obtained that offers a more concise description of the physical processes responsible for the propagation of anomalous precipitation. The precipitation budget differs from traditional moisture or moist static energy budgets in that it emphasizes the regions where precipitation is most sensitive to changes in moisture.

We will use the methodology of Adames and Wallace (2014a,b, 2015, hereafter AW1, AW2, and AW3, respectively) and Adames et al. (2016, hereafter AWM) in order to further understand the evolution of the MJO-related precipitation anomalies. These four studies were based on regression maps in which the daily 850- minus 150-hPa velocity potential field was used as a time-varying MJO index. A particular focus will be placed on the "warm pool" compositing technique, which yields a cleaner and more concise description of the most salient features of the MJO as it propagates across the warm pool. The results of this study expand on the results of AW3 by further revealing the role that the vertical profile of vertical velocity plays the propagation of the MJO along the equatorial band (10°N–10°S). The profile of ascent is, in turn, intrinsically related to shallow meridional circulations associated with the easterly and westerly wind anomalies in the Kelvin and Rossby waves described in AW2. These circulation features also induce propagation of the MJO through horizontal moisture advection.

The structure of this paper is as follows. The next section describes the datasets and methods of analysis. Section 3 describes a prognostic precipitation budget for the MJO. Section 4 discusses the mechanism that maintain the MJO-related precipitation anomalies and the mechanisms that lead to its eastward propagation. A concluding discussion is offered in section 5.

2. Data and methods

Four datasets are used in this study. We make use of the 1.5° longitude × 1.5° latitude horizontal-resolution, daily column-integrated, and pressure-level fields in the ERA-Interim dataset (Dee et al. 2011), for the time period 1979–2011. The horizontal wind components u and v are used in this study as field variables and in the calculation of velocity potential χ. Specific humidity q and vertical velocity ω are also used as field variables in this study. Temperature T is used in the calculation of the saturation specific humidity q_s in sections 3 and 4. Furthermore, we make use of ERA-Interim precipitation P. The surface and top-of-the-atmosphere longwave radiative heating fields are also used in the calculation of the column longwave radiative heating (LW′). Fields involving products of individual ERA-Interim variables are also used in section 4. These products are calculated from each daily averaged field, as in AW3 and AWM, and afterward the procedure is the identical to the analysis of the individual field variables.

We also make use of daily averaged precipitation from the 3B42, version 7, product of the Tropical Rainfall Measurement Mission (TRMM-3B42, Huffman et al. 2007, based on the period 1998–2011). The dataset is interpolated to 1.5° longitude × 1.5° latitude horizontal resolution to facilitate comparison with the ERA-Interim data and in the calculation of the convective adjustment time scale.

The fields used in this study correspond to MJO-related anomalies. We obtain these by removing the mean and first three harmonics of the annual cycle based on the 1979–2011 reference period. Additionally, a 101-point Lanczos filter (Duchon 1979) is used to extract the anomalies that occur within 20–100-day time scales.

The fields described in this study are regression maps, obtained using the methods of AW1, AW2, and AW3. These are obtained through the following equation:

$$\mathbf{D} = \mathbf{S}\hat{\mathbf{P}}^{\mathrm{T}}/N,$$

where $\mathbf{D}$ is the linear regression for a two-dimensional matrix $\mathbf{S}$, which represents a field variable S. The

regression map is obtained by projecting **S** upon a standardized MJO index $\hat{\mathbf{P}}$ and dividing by the number of days N. Most of the patterns shown here are obtained by regressing fields upon linear combinations of the two leading principal components (PCs) of daily mean global fields of 850- minus 150-hPa velocity potential $\Delta\chi$. A comprehensive description of this index is presented in AW1, along with a comparison of its performance with that of other MJO indices. Contour and shading intervals in the plots presented here are scaled to the approximate value of the 95% confidence interval based on a two-sided t test.

The modal vertical profiles for vertical velocity ω_1 and ω_2, shown in Fig. 6 of AW2, are also used in this study: ω_1 corresponds to a vertical velocity profile in which perturbations of the same polarity extend through the depth of the troposphere, with a midtropospheric ($\sim$400 hPa) maximum, and ω_2 corresponds to a profile in which the vertical velocity perturbations are of opposing polarity above and below the 600-hPa level. Vertical velocity ω_1 is an overall measure of the strength of the convection, and ω_2 is useful for distinguishing between shallow convection and elevated stratiform convection, as discussed by Houze (1982) and Schumacher et al. (2004), among others.

Many of the fields shown in section 4 are "warm pool composites," generated using the analysis technique described in AW2, AW3, and AWM. The composites are constructed by generating a series of regression maps based on linear combinations of PC1 and PC2 of $\Delta\chi$ for the MJO phases in which the $\Delta\chi$ maximum is centered over the Indo-Pacific warm pool (60°E–180°). A warm pool composite corresponding to the time when the MJO is active over the Maritime Continent (maximum PC1, denoted WPC1) is generated by zonally shifting each member of the sequence of maps such that the longitude at which $\Delta\chi$ is a maximum corresponds to the reference longitude (0°). A composite that corresponds to the time when the MJO is active over the Indian Ocean (minimum PC2, denoted WPC2) is also constructed. In this composite, the reference longitude corresponds to the node in $\Delta\chi$ in which $\partial\Delta\chi/\partial x$ is negative. Together, WPC1 and WPC2 can be thought of representing the MJO cycle as it propagates eastward across the Indo-Pacific warm pool.

3. A moisture-based precipitation budget

Many of the studies that attempt to understand the eastward propagation of the MJO have focused either on the intraseasonally filtered (20–100-day bandpass-filtered) moisture or moist static energy budget. The vertically integrated intraseasonal moisture equation takes the following form:

$$\frac{\partial \langle q' \rangle}{\partial t} = -\langle \mathbf{V} \cdot \nabla q \rangle' - \left\langle \omega \frac{\partial q}{\partial p} \right\rangle' - P' + E', \qquad (1)$$

where primes correspond to intraseasonal (20–100-day time scale) anomalies, and the primed angle brackets denote the mass-weighted vertical integral of the anomaly fields

$$\langle \mathbf{V} \cdot \nabla q \rangle' = \frac{1}{g} \int_{100\text{hPa}}^{1000\text{hPa}} (\mathbf{V} \cdot \nabla q)' \, dp. \qquad (2)$$

One of the goals of this study is to transform Eq. (1) into a prognostic equation for the intraseasonal precipitation anomalies, which requires an equation that relates column water vapor and precipitation. An empirical equation that relates column relative humidity to precipitation was obtained by Bretherton et al. (2004), which is of the following form:

$$P(R_h) = P_0 \exp(aR_h), \qquad (3)$$

where $R_h = \langle q \rangle / \langle q_s \rangle$ is the column relative humidity, and P_0 and a are constants, a corresponding to a "sensitivity" parameter of precipitation with respect to R_h. A similar relationship was also found by Raymond (2000) and Peters and Neelin (2006). Physically, the relationship is related to the dilution that updrafts experience in the free troposphere. When environmental humidity is high, cloud water evaporates less and cloud buoyancy is reduced less by the impact of entrainment (Raymond 2000; Holloway and Neelin 2009), which leads to greater organization of convection (Masunaga 2012; Ahmed and Schumacher 2015). As shown by Yasunaga and Mapes (2012), the relationship between moisture and precipitation is most coherent at the spectral bands corresponding to the MJO (20–100-day time scales, eastward-propagating zonal wavenumbers 1–5).

An example of this relationship for a region in the equatorial Indian Ocean is shown in Fig. 1a. While there is a large scatter between precipitation and column relative humidity, it is clear that the relationship is approximately exponential, with a sharp pickup in precipitation at $R_h \sim 0.75$. A similar relation is found in ERA-Interim precipitation (Fig. 1b), although in this case the pickup at high R_h is weaker, corresponding to a smaller a. The cluster of points in the scatterplots can be separated into groups that correspond to days in which PC2 of $\Delta\chi$ exceeded 1.5 and -1.5, indicative of suppressed and active MJO convection over the Indian Ocean, respectively. The separation clearly shows that
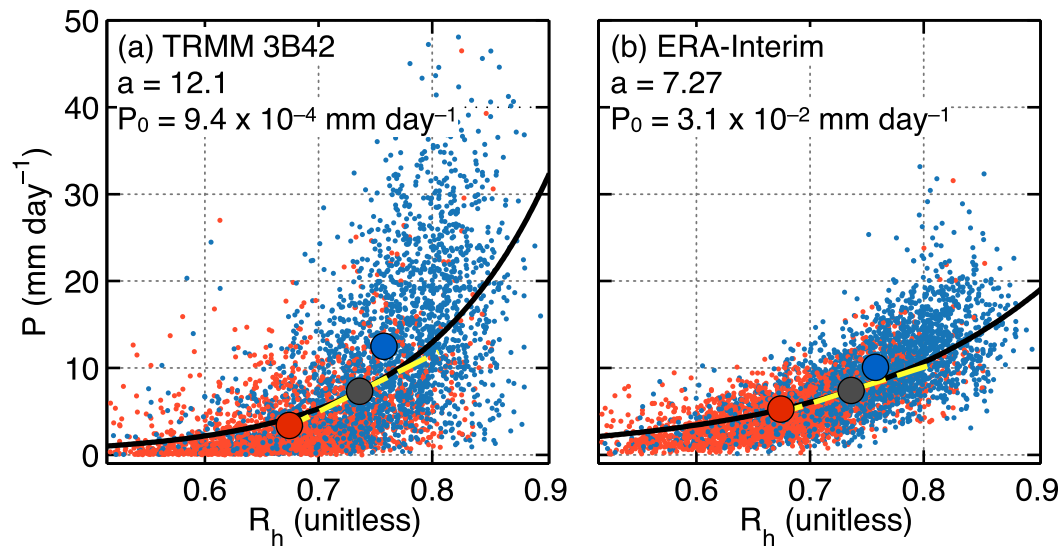
FIG. 1. (a) Scatterplot of TRMM 3B42 precipitation P as a function of ERA-Interim column relative humidity R_h averaged over a 5° box centered over the equator at 95°E. The black line depicts the nonlinear least squares fit of the points in the scatterplot. The dashed yellow line shows the Taylor series linearization [Eq. (7)] of the exponential fit for a reference relative humidity profile of $\overline{R_h} = 0.74$, centered on the gray circle. Red dots correspond to days in which PC2 of $\Delta\chi$ is greater than 1.5 while blue dots correspond to days in which PC2 of $\Delta\chi$ is less than −1.5. PC2 of $\Delta\chi$ corresponds to the time when convection is enhanced/suppressed over the Indian Ocean. The large red and blue circles correspond to the centroids of the red and blue cluster of points, respectively. (b) As in (a), but for ERA-Interim precipitation.

the most humid and rainy days correspond to days when the MJO is active over the Indian Ocean. Conversely, the driest days correspond to days when MJO convection is suppressed.

The horizontal distribution of annual-mean precipitation, its standard deviation, and the annual-mean column relative humidity are shown in Figs. 2a–c. All three fields exhibit qualitatively similar patterns, implying

that, to first order, precipitation variability is proportional to the low-frequency background state.

Based on the correspondence between the low-frequency precipitation, R_h, and precipitation variability, we can expand Eq. (3) into a Taylor series centered on a slowly varying background column relative humidity $\overline{R_h}$ value, where the overbars denote a 100-day low-pass filter. By truncating the series on its second
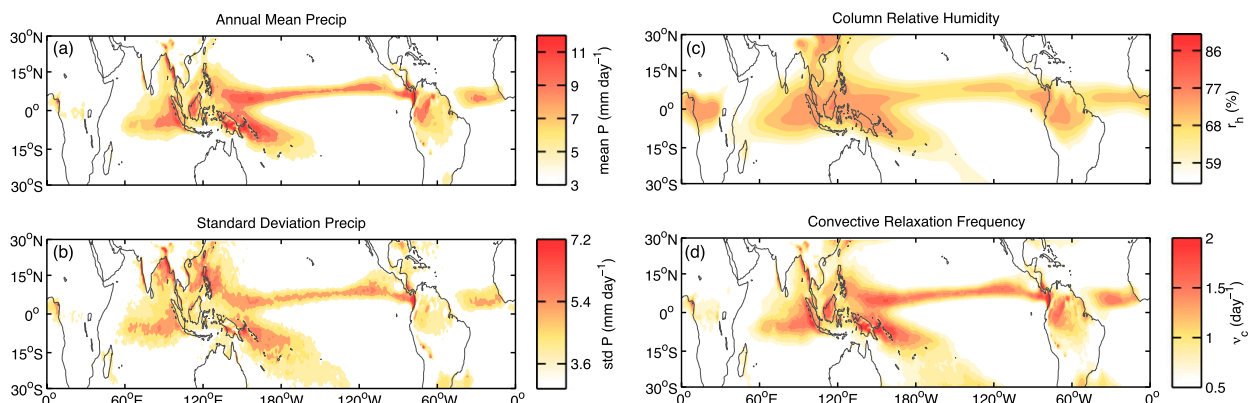
FIG. 2. Spatial distributions of annual-mean (a) TRMM 3B42 precipitation $\overline{P}$, (b) standard deviation of 20–100-day-filtered TRMM 3B42 precipitation, (c) ERA-Interim column relative humidity $\overline{R_h}$, and (d) the convective relaxation frequency $\overline{\nu_c}$. For the calculation of $\overline{\nu_c} = a\overline{P}/\langle\overline{q_s}\rangle$, TRMM 3B42 precipitation is used, where $a = 12.1$. For the calculation of $\overline{\nu_c}$, the fields were low-pass filtered to retain time scales longer than 100 days. The annual-mean distribution of $\overline{\nu_c}$ was obtained by averaging the low-pass-filtered $\overline{\nu_c}$.
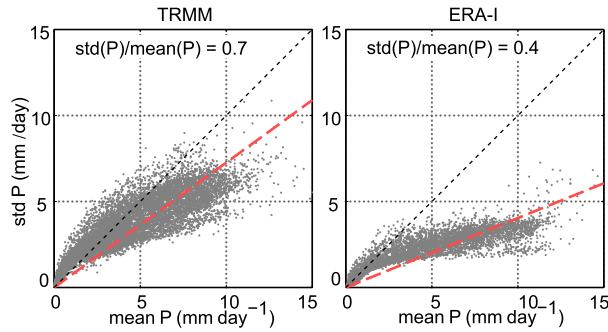
FIG. 3. Scatterplots of standard deviation of 20–100-day-filtered precipitation vs annual-mean precipitation from (left) TRMM-3B42 and (right) ERA-Interim. The 1:1 line is shown as a black dashed line and the linear least squares fit is shown as a red dashed line.

term, we obtain the following linearized equation for precipitation:

$$P(R_h) \simeq \overline{P}(\overline{R_h}) + R_h' \frac{\partial P}{\partial R_h}\Big|_{R_h = \overline{R_h}}, \qquad (4)$$

where $R_h' = R_h - \overline{R_h}$ is the relative humidity perturbation. An example of this linear approximation is shown as a dashed line in Fig. 1. The equation states that total precipitation is approximately a function of $\overline{R_h}$, modulated by small perturbations. If the saturation column water vapor is assumed to vary slowly in time (at seasonal time scales, $\langle q_s \rangle \simeq \langle \overline{q_s} \rangle$), it follows that intraseasonal perturbations in relative humidity are approximately determined by changes in the column water vapor content, $R_h' = \langle q' \rangle / \langle \overline{q_s} \rangle$. With the aforementioned relation and using Eq. (3) to define $\overline{P} = P_0 \exp(a\overline{R_h})$, Eq. (4) can be simplified to

$$P \simeq \overline{P}\left(1 + a \frac{\langle q' \rangle}{\langle q_s \rangle}\right). \qquad (5)$$

The precipitation anomalies can be rewritten in the following form:

$$P' \simeq a \frac{\overline{P}}{\langle \overline{q_s} \rangle} \langle q' \rangle, \qquad (6)$$

which shows that the amplitude of the intraseasonal precipitation anomalies are, to first order, directly related to the amplitude of the low-frequency background precipitation. Furthermore, the importance of the precipitation sensitivity parameter a becomes clearer, as it determines the magnitude of precipitation variability. This relation shows that moisture-driven precipitation perturbations are more relevant over the climatologically rainy regions of the tropics. Figure 3 shows the

relationship between annual-mean precipitation $\overline{P}$ and the standard deviation of 20–100-day-filtered precipitation. While the relationship is not perfectly linear, it is clear that intraseasonal variations in precipitation increase as climatological-mean precipitation increases. In comparison, ERA-Interim precipitation exhibits a much weaker relationship, with precipitation variability nearly plateauing after ~3 mm of annual-mean precipitation. Thus, while both datasets show a relationship between P' and $\overline{P}$, TRMM data exhibits a larger sensitivity parameter a than ERA-Interim data does, consistent with Fig. 1.

Some of the terms on the right-hand side of Eq. (6) can be used to define a low-frequency background convective adjustment time scale:

$$\overline{\tau}_c = \frac{\langle \overline{q_s} \rangle}{a\overline{P}}, \qquad (7)$$

which can be thought of as the time scale for anomalous precipitation to relax R_h back toward its climatological value. This time scale is analogous to the one used in the simplified Betts–Miller convective adjustment scheme (Betts and Miller 1986; Betts 1986; Frierson 2007), except $\overline{\tau}_c$ exhibits horizontal variations here. Here, $\overline{\tau}_c$ determines the strength of a precipitation response to anomalous water vapor.

Equation (7) indicates that $\overline{\tau}_c$ is smallest over the climatologically rainy regions and tends toward infinity over the dry regions of the tropics. Because of this sensitivity to $\overline{P}$, it may be useful to define a convective relaxation frequency:

$$\overline{\nu}_c = \frac{1}{\overline{\tau}_c}. \qquad (8)$$

The horizontal distribution of $\overline{\nu}_c$ is shown in Fig. 2d, using ERA-Interim values $\langle \overline{q_s} \rangle$ and TRMM 3B42 values of $\overline{P}$ (interpolated onto the ERA-Interim grid). A value of a of 12.1 is used, which is obtained from a nonlinear least squares fit of the cloud of points of TRMM $\langle q \rangle$ and P across the warm pool (10°N–10°S, 60°E–180°). This value of a is smaller than the value of 15.6 obtained by Bretherton et al. (2004) using daily data, which may be a result of the datasets used here. It is clear that $\overline{\nu}_c$ shows a nearly identical distribution to the climatological-mean precipitation. This is due to $\langle \overline{q_s} \rangle$ exhibiting relatively little variation in the tropics, consistent with the notion that tropical temperature gradients are weak (Sobel and Bretherton 2000; Sobel et al. 2001). The spatial distribution of $\overline{\nu}_c$ is also consistent with the spatial distribution of intraseasonal precipitation variability, shown in Fig. 2c. It will be shown later that the intraseasonal
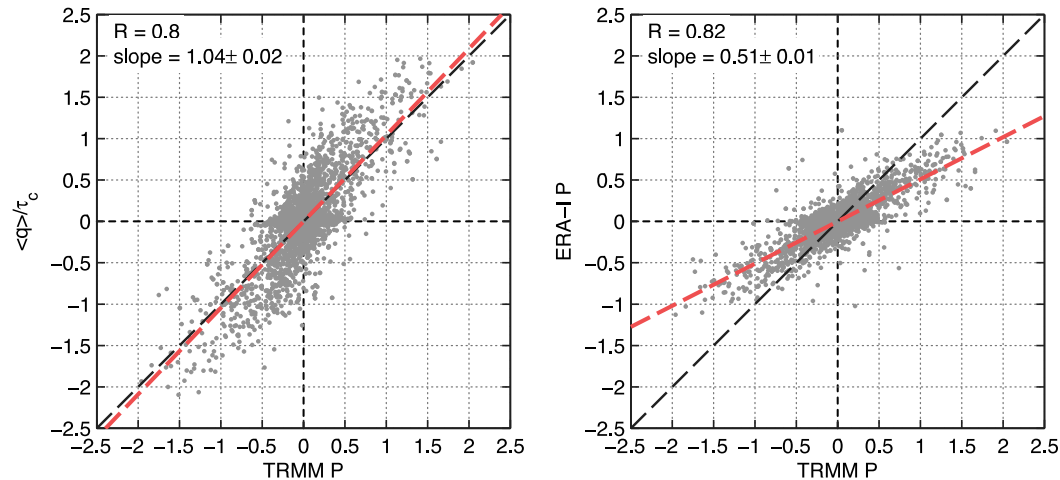
FIG. 4. Scatterplots of TRMM 3B42 precipitation anomalies vs (left) estimated precipitation $P' = \langle q' \rangle / \overline{\tau_c}$ and (right) ERA-Interim precipitation, regressed onto PC1 and PC2 of $\Delta\chi$. The fields are averaged over the Indo-Pacific warm pool (15°N–15°S, 60°E–180°). The 1:1 line is shown as a black dashed line. The linear fit obtained from linear least squares fit is shown as a red line. The correlation coefficient and the slope of the linear fit are shown in the top-left corner of each panel. For the calculation of $\overline{\tau_c}$, TRMM-3B42 precipitation is used and $a = 12.1$, as obtained from the nonlinear least squares fit. Only points occurring over the oceans have been included.

precipitation tendency $\partial P'/\partial t$ is directly related to $\overline{\nu_c}$. Thus, intraseasonal precipitation variability (Fig. 2b) will be largest in regions where $\overline{\nu_c}$ is large.

To further verify the validity of the aforementioned approximation to the analysis of the structure and evolution of the MJO, Fig. 4a compares the derived precipitation field $P' = \langle q' \rangle / \overline{\tau_c}$ to precipitation estimates from TRMM-3B42. The scatterplots are obtained from linear regression of the fields onto PC1 and PC2 of $\Delta\chi$ (see appendix), averaging all points over the equatorial belt (15°N–15°S, 60°E–180°). Only points occurring over the oceans were included, as precipitation over land may be modulated by other processes, such as the diurnal cycle and orography (Peatman et al. 2014; Birch et al. 2016, see their Fig. 13). A robust relationship is observed between the two fields, with a correlation coefficient of ~0.8 and a slope of 1.04. Compared to the precipitation output from ERA-Interim (right panel), the linearized precipitation yields a more realistic and robust distribution of precipitation for the MJO, with a similar correlation coefficient and a slope close to unity.

Figure 5 compares the horizontal structure of the derived P' with TRMM-3B42 P' for the warm pool composite corresponding to the time when the MJO-related $\Delta\chi$ anomalies are centered over the Maritime Continent (WPC1, top panel) and at the time when the MJO-related $\Delta\chi$ anomalies are centered over central Indian Ocean (WPC2, bottom panel). The derived P' robustly captures all of the major features seen in TRMM-3B42, with only some minor differences. These differences include

TRMM-3B42 precipitation being slightly shifted westward with respect to the derived P' in WPC1. In WPC2, the derived P' is too large compared to TRMM over the bands of the ITCZ and over the SPCZ.

With the aforementioned approximations, we can turn Eq. (1) into a precipitation budget by scaling it by $\overline{\tau_c}$:

$$\frac{\partial P'}{\partial t} \simeq \frac{1}{\overline{\tau_c}} (-\langle \mathbf{V} \cdot \nabla q \rangle' + C'), \tag{9}$$

where we have incorporated the sum of vertical moisture advection, surface latent heat fluxes, and precipitation as the so-called column-process term (Chikira 2014; Wolding and Maloney 2015; Janiga and Zhang 2016):

$$C' = -\left\langle \omega' \frac{\partial \overline{q}}{\partial p} \right\rangle - P' + E'. \tag{10}$$

Since horizontal and temporal variations of temperature are weak in the tropics, we can apply the weak temperature gradient approximation (Charney 1963; Sobel and Bretherton 2000; Sobel et al. 2001). Under this approximation, it is assumed that buoyancy perturbations T' due to convection are smoothed out by the energy dispersion in gravity waves, whose time scales are much shorter than the MJO. This process is known as "gravity wave adjustment" (Wolding and Maloney 2015) or "buoyant equalization" (Bretherton and Smolarkiewicz 1989). In combination with the
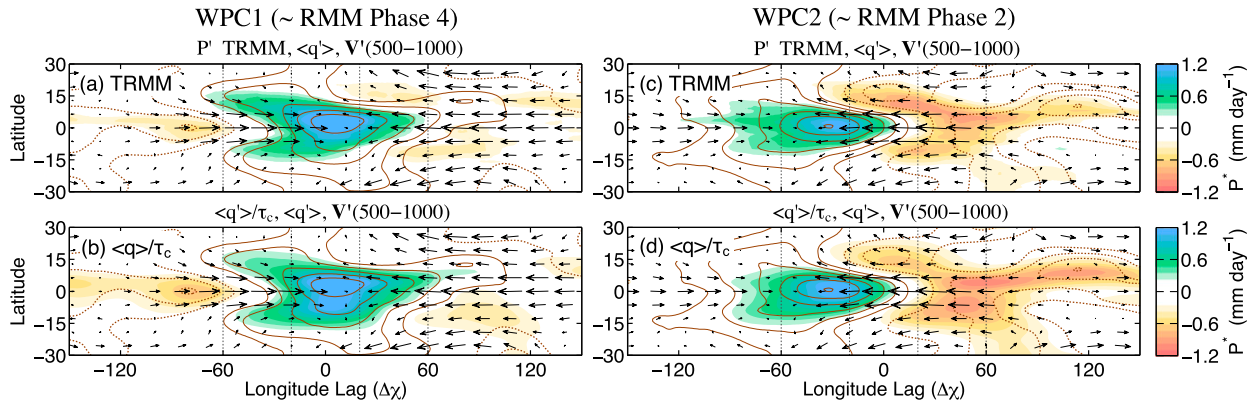
FIG. 5. (left) Warm pool composite centered over the Maritime Continent (WPC1) and (right) warm pool composite centered over the central Indian Ocean (WPC2) of (a),(c) TRMM-3B42 precipitation and (b),(d) estimated precipitation $P' = \langle q' \rangle / \overline{\tau_c}$. Column water vapor $\langle q' \rangle$ is shown as contours (contour interval: 0.15 mm) and the 500–1000-hPa-averaged wind field is shown as arrows (largest wind vector is $\sim 1\,\mathrm{m\,s^{-1}}$). For the calculation of $\overline{\tau_c}$, ERA-Interim mean precipitation is used and $a = 12.1$, as obtained from the nonlinear least squares fit. Note that for WPC1 the reference longitude corresponds to the maximum in $\Delta\chi$ (850–150-hPa velocity potential), and in WPC2 the reference longitude corresponds to the node in $\Delta\chi$.

large Rossby radius of deformation that arises from the weak planetary vorticity characteristic of the equatorial latitudes, these gravity wave responses to convection homogenize the horizontal free-tropospheric temperature distribution. As a result, the leading balance in the intraseasonal thermodynamic energy equation is between anomalous diabatic heating and cooling from adiabatic expansion induced by anomalous ascent:

$$\omega' \frac{\partial \overline{s}}{\partial p} \simeq Q_1', \tag{11}$$

where Q_1' is the intraseasonal diabatic heating anomaly, and $\overline{s}$ is the low-frequency background mean dry static energy. Note that fields with overbars correspond to 100-day low-pass-filtered data. It was shown by Wolding et al. (2016) that this approximation is valid at intraseasonal time scales. We have neglected the contribution of advection of anomalous dry static energy by the mean vertical motion field and the nonlinear eddy term since their column-integrated contributions are small (not shown). Since the main contributors to diabatic heating Q_1 arise from convective and radiative heating, we can separate the anomalous vertical velocity into a radiatively driven component ω_r' and a component driven by anomalous convective processes and large-scale vertical motion ω_c':

$$\omega_r' \simeq Q_r' \left(\frac{\partial \overline{s}}{\partial p} \right)^{-1} \quad \text{and} \tag{12a}$$

$$\omega_c' \simeq Q_c' \left(\frac{\partial \overline{s}}{\partial p} \right)^{-1}. \tag{12b}$$

With this separation, we can now define a "convectively driven" column process, which includes the contribution to ascent by microphysical processes and eddies of scales smaller than those resolved by the reanalysis

$$C_c' = -\left\langle \omega_c' \frac{\partial \overline{q}}{\partial p} \right\rangle - P', \tag{13}$$

which can be thought of as the net moistening/drying by vertical moisture advection due to convection and large-scale dynamics. It is related to the vertical gross moist stability (Neelin and Held 1987; Raymond et al. 2009; Inoue and Back 2015). A positive C_c' implies an unstable profile where convection moistens the atmosphere, "preconditioning" it for further convection, consistent with a negative gross moist stability as defined in their studies. When C_c' is negative, moisture is lost to condensation and precipitation, inhibiting the subsequent development of convection, indicative of a positive gross moist stability. With the aforementioned approximations, the precipitation budget can be rewritten in the following form:

$$\frac{\partial P'}{\partial t} \simeq \frac{1}{\overline{\tau_c}} \left(-\langle \mathbf{V} \cdot \nabla q \rangle' - \left\langle \omega_r' \frac{\partial \overline{q}}{\partial p} \right\rangle + E' + C_c' \right). \tag{14}$$

Equation (14) is the linearized version of Eq. (9) in Inoue and Back (2015), which describes the slow temporal evolution of precipitation due to changes in the ambient relative humidity (by changes in column water vapor). That is, precipitation slowly increases in environments that are becoming more moist and decreasing in environments that are drying. The scaling by $\overline{\tau_c}$ is used

since moist environments are more sensitive to changes in relative humidity than dry environments, as shown in Figs. 1 and 2.

It is worth noting that if $\overline{\tau_c}$ is assumed a constant in space, and assuming that the propagation of the precipitation anomalies is determined by the wind anomalies in the Matsuno-Gill response to an equatorial heat source (Matsuno 1966; Gill 1980), then a linear wave solution to Eq. (14) can be obtained, as in Adames and Kim (2016). In this study we will show that spatial variations in $\overline{\tau_c}$ causes the spatial distribution of anomalous precipitation to differ somewhat from the horizontal pattern in column moisture. This will in turn lead to a change in the relative importance of different dynamical processes to the eastward propagation of the MJO than by solely considering a moisture or moist static energy budget.

4. Precipitation maintenance and evolution in a composite MJO

In this section, we perform a comprehensive analysis of the spatial distribution of precipitation field in the MJO and the dynamical processes responsible for its maintenance and evolution. However, it is important to understand how the estimated precipitation field P' differs from the column-integrated water vapor anomalies $\langle q' \rangle$. Figure 5 compares the precipitation field with $\langle q' \rangle$ in WPC1 and 2. The fields P' and $\langle q' \rangle$ exhibit similar horizontal structures, with the characteristic "swallowtail" shape in WPC1 identified by Zhang and Ling (2012) and described in AW2 and AW3. However, P' is meridionally narrower than $\langle q' \rangle$. Also, P' is strongest in the regions that correspond to the equatorial warm pool, and along the narrow bands of the ITCZ, consistent with the distribution of $\overline{\nu_c}$ in Fig. 2.

To understand how P' evolves throughout the MJO cycle, Fig. 6 shows the local tendency in precipitation $\partial P'/\partial t$, and the contribution to this tendency by horizontal moisture advection and column processes C', following Eq. (9). The patterns are similar to those seen in the moisture budget in AW3, but more equatorially focused. In WPC1, column processes dominate the moistening to the east of the rain area while horizontal moisture advection is the dominant sink to the west. The pattern in WPC2, which shows a large positive precipitation tendency in the node of the dipole in enhanced and suppressed convection (near the reference longitude) has substantial contributions from both horizontal moisture advection and C'. It is noteworthy that C' are a larger contributor near the equator ($\sim$10°N–10°S) while horizontal moisture advection is a larger contributor away from the equator (poleward of 10°N/S).

As in Maloney (2009), Kiranmayi and Maloney (2011), and Kim et al. (2014a), among others, we decompose the horizontal moisture advection field into a term describing the horizontal advection of low-frequency moisture by the MJO winds, a term describing the advection of MJO moisture by the background winds, and a third term representing the nonlinear advection of moisture by eddies of time scales shorter than 20 days:

$$-\langle \mathbf{V} \cdot \nabla q \rangle' \simeq -\langle \mathbf{V}' \cdot \nabla \overline{q} \rangle' - \langle \overline{\mathbf{V}} \cdot \nabla q' \rangle' - \langle \mathbf{V}'' \cdot \nabla q'' \rangle',$$

(15)

where the double primes denote fields that have been high-pass filtered to retain time scales shorter than 20 days. Other terms also contribute to the total horizontal advection field, but they are negligibly small when compared to the leading three terms above (not shown). The separated contributions to horizontal advection are shown in Fig. 7. Scaling by $\overline{\tau_c}$ leads to a reduction in the contribution of the advection of mean moisture by the anomalous winds (see Fig. A1 in AW3 for comparison). Instead, it is the nonlinear contribution to drying by high-frequency eddy activity which exhibits the largest magnitude. These are observed near and to the west of the precipitation anomalies and are dominated by its zonal wind contribution (see Fig. 8 of AW3). In contrast, $-\langle \mathbf{V}' \cdot \nabla \overline{q} \rangle$ exhibits a horizontal structure that is in quadrature with the rain area in WPC1, while it acts to broaden the rain area in WPC2. Advection of moisture by the mean flow contributes little to the propagation of the intraseasonal precipitation anomalies in these 12-month-based composites.

Figure 8 decomposes the anomalous column processes C' into the individual contributions from surface latent heat fluxes E', radiatively driven vertical moisture advection $\omega_r' \partial \overline{q}/\partial p$, and the convectively driven column processes C_c', which are obtained as the residual of the precipitation budget. In both WPC1 and WPC2, anomalous surface latent heat fluxes is anticorrelated with the precipitation tendency, indicating that it acts to slow down the propagation of the precipitation anomalies, consistent with previous studies (Kim et al. 2014a; Sobel et al. 2014). The strongest anomalies are collocated with the zonal wind anomalies; that is, surface latent heat fluxes are enhanced in regions of westerlies and suppressed in regions of easterly flow. The contribution of radiation, which is dominated by longwave heating, can be approximately estimated from the ERA-Interim column longwave radiation (LW') by projecting it to the first baroclinic mode in vertical motion ω_1:

$$\left\langle \omega_r' \frac{\partial \overline{q}}{\partial p} \right\rangle \simeq \left\langle \hat{\omega}_1 \frac{\partial \overline{q}}{\partial p} \right\rangle \left\langle \hat{\omega}_1 \frac{\partial \overline{s}}{\partial p} \right\rangle^{-1} \mathrm{LW}', \qquad (16)$$

where $\hat{\omega}_1$ is the normalized vertical structure function for ω_1 (see Fig. 6 of AW2), which describes deep
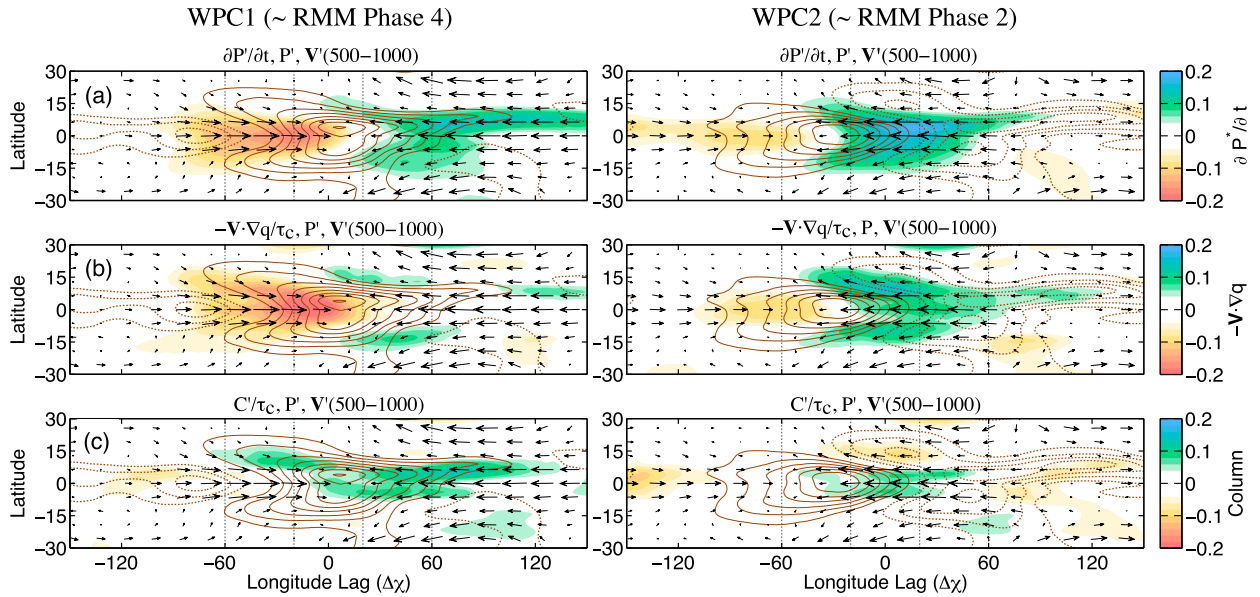
FIG. 6. (left) WPC1 and (right) WPC2 of (a) the precipitation tendency $\partial P'/\partial t$ and the contribution to precipitation changes by (b) horizontal moisture advection and (c) column processes (the sum of vertical moisture advection and precipitation). The precipitation rate $P' = \langle q' \rangle / \overline{\tau_c}$ and the 500–1000-hPa-averaged wind field are shown as contours (contour interval: 0.05 mm day^{-1}) and arrows (largest wind vector is ~1 m s^{-1}), respectively.

convective ascent. The two terms in the right-hand side of Eq. (16) correspond to the gross moisture stratification divided by the gross dry stability, respectively (Neelin and Zeng 2000). The contribution of OLR to the precipitation tendency is comparable to that of surface latent heat fluxes but is collocated with the precipitation anomalies, albeit shifted westward. It is strongest at the

time when the MJO-related anomalies are crossing the Maritime Continent (WPC1), indicating that anomalous cloud cover in the upper troposphere is a maximum at that time.

The contribution of convective column processes C_c' is shown in the bottom panel of Fig. 8. This term is calculated as the residual from the sum of the other terms
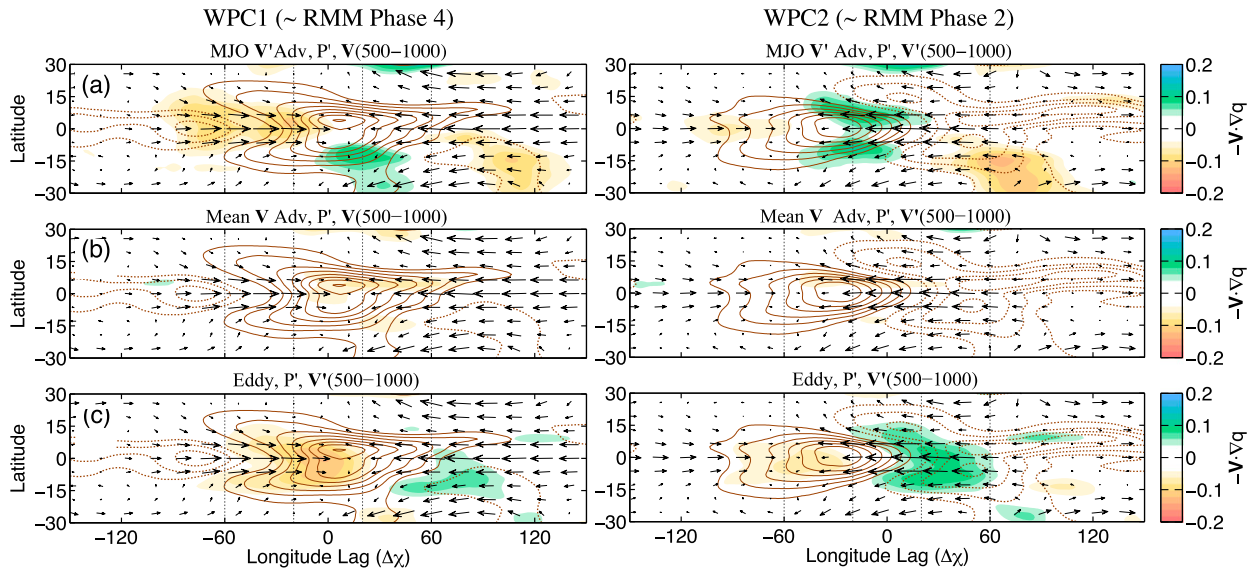
FIG. 7. As in Fig. 6, except the shaded fields depict (a) horizontal advection of low-frequency moisture by the MJO winds $-\langle \mathbf{V}' \cdot \nabla \overline{q} \rangle'$, (b) horizontal advection of MJO moisture by the low-frequency flow $-\langle \overline{\mathbf{V}} \cdot \nabla q' \rangle'$, and (c) horizontal moisture advection by high-frequency eddy activity $-\langle \mathbf{V}'' \cdot \nabla q'' \rangle'$.
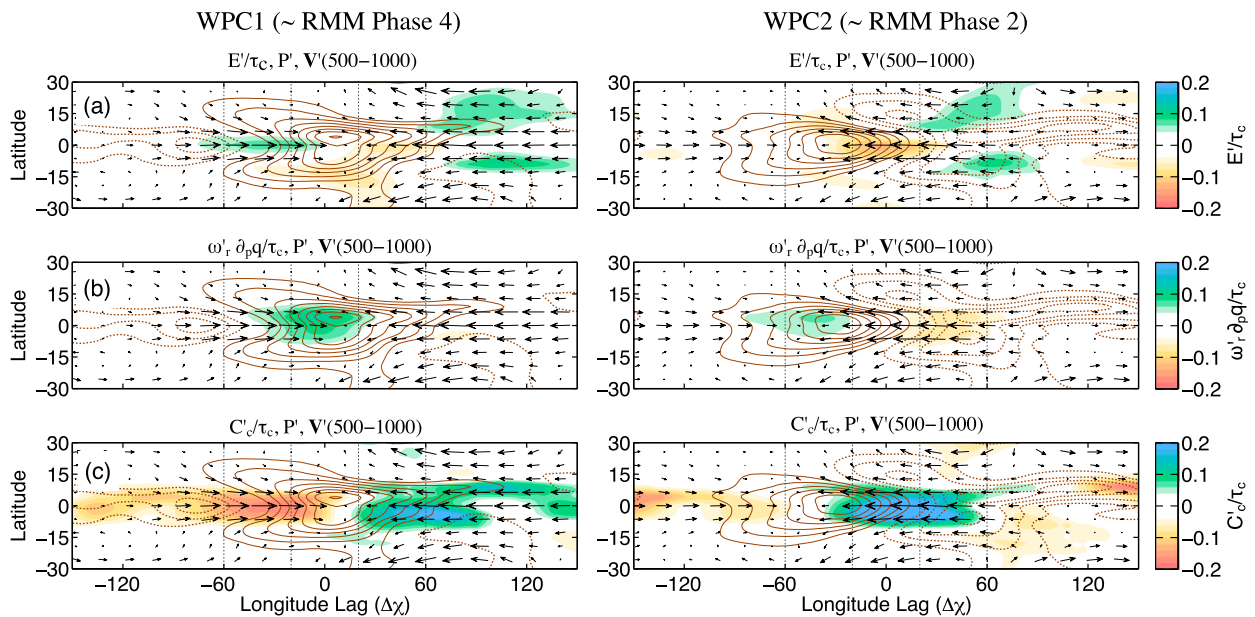
FIG. 8. As in Fig. 6, except the shaded fields depict (a) anomalous surface latent heat fluxes E', (b) vertical moisture advection due to longwave radiative heating $\omega'_r \partial \overline{q}/\partial p$, and (c) moistening arising from convective column processes C'_c.

Eq. (14). While a significant residual in the ERA-Interim moisture budget has been previously documented, it has been attributed to the vertical advection of moisture and its associated apparent moisture sink due to the convective parameterization used in the reanalysis (Kiranmayi and Maloney 2011; Mapes and Bacmeister 2012; AW3). The anomalies in C'_c are in phase with the zonal wind anomalies, with moistening occurring in regions of anomalous easterlies and drying in westerlies. It is strongest at the time of WPC2, when the superposition of the Kelvin wave response from the enhanced convection ~30° to the west of the reference longitude and the Rossby wave response to the suppressed convection ~60° to the east of the reference longitude cause the easterly wind anomalies to be a maximum. The horizontal distribution in C'_c is reminiscent to the distribution of the second baroclinic mode in vertical motion ω_2 (Fig. 7 in AW2). Vertical motion ω_2 is characterized by perturbations of opposing polarity above and below 600 hPa. A positive ω_2 describes a profile of ascent that is shallow while a negative ω_2 describes elevated stratiform ascent.

To further analyze the cause of the net moistening and drying induced by C'_c, we will decompose the ω field into ω_1 and ω_2, as in AW2, and analyze their contributions to vertical moisture advection, shown in Fig. 9. Vertical moisture advection by ω_1 (middle panel) exhibits nearly the same structure as the total vertical moisture advection (top panel), both occurring over the precipitation region. Advection by ω_2, while only ~1/3 as large as the

contribution by ω_1, exhibits a nearly identical spatial pattern as C'_c, albeit with a larger amplitude. This result suggests that vertical moisture advection by ω_2 is an important contributor to the precipitation tendency near the equator; that is

$$C'_c \propto \left\langle \omega'_2 \frac{\partial \overline{q}}{\partial p} \right\rangle; \tag{17}$$

that is, in regions where the profile of ascent is shallow, moist boundary layer air is advected to the lower free troposphere, leading to tropospheric moistening and increasing precipitation. In regions of elevated stratiform ascent, the precipitation tendency is dominated by anomalous descent occurring beneath the 600-hPa level, which dries out the lower free troposphere. This moistening and drying likely results both from vertical motion in association with wave motion (Wang and Rui 1990) as well as thermodynamic feedbacks involving cloud detrainment and rain reevaporation, as discussed by Chikira (2014). A similar result was found by Wolding et al. (2016). Their Fig. 7d shows strong moistening to the east in the lowermost layer of the free troposphere and drying over the region where the moisture anomalies are a maximum, consistent with a vertical profile of ascent akin to ω_2.

We can assess the relative importance of the terms in Eq. (14) to the maintenance and evolution of the MJO-related precipitation regions. Following the method
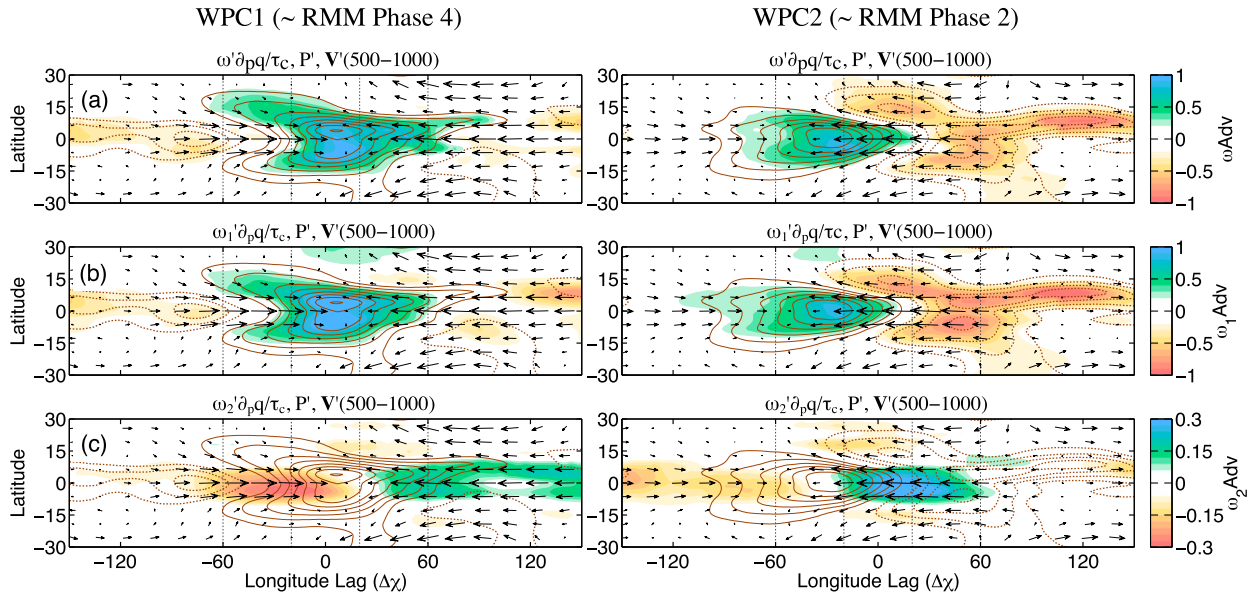
FIG. 9. As in Fig. 6, except the shaded fields depict (a) column-integrated vertical moisture advection $\omega' \partial \overline{q}/\partial p$, (b) column-integrated vertical moisture advection due to deep convective ascent $\omega_1' \partial \overline{q}/\partial p$, and (c) column-integrated vertical moisture advection due to shallow/stratiform ascent $\omega_2' \partial \overline{q}/\partial p$.

used by Andersen and Kuang (2012), Arnold et al. (2013), and AWM, we compare the strength of their projections upon the horizontal distribution of precipitation and its temporal tendency

$$S_t(F) = \frac{\|F \cdot \partial P'/\partial t\|}{\|\partial P'/\partial t \cdot \partial P'/\partial t\|} \quad \text{and} \quad (18a)$$

$$S_m(F) = \frac{\|F \cdot P'\|}{\|P' \cdot P'\|}, \quad (18b)$$

where F is each individual term in Eq. (14). Thus, Eqs. (18a) and (18b) are evaluated for every term in Eq. (14), and $\|(\cdots)\|$ is the integral of $(\cdots)$ over the domain 15°N–15°S and within 100° of the reference longitude.

The results, shown in Fig. 10, reveal several differences when compared to simply using a column moisture budget. First, because precipitation is most sensitive to changes in water vapor near the climatologically rainy areas of the warm pool, near-equatorial moist processes project more strongly to P' and $\partial P'/\partial t$ than off-equatorial processes. As a result, meridional advection of mean moisture by the anomalous winds plays a smaller role in the propagation of P' than what a column moisture budget suggests. Instead, the largest contributor to the eastward propagation of P' is C_c', which was shown in Fig. 9 to be closely related to ω_2. This large contribution arises when the contributions of longwave radiation and surface latent heat fluxes to the column processes are considered separately, both of which

act to slow down the eastward propagation of the MJO. The contribution of horizontal moisture advection to propagation is not dominated by a single term; rather, it is composed by interactions between several temporal scales. When all the horizontal moisture advection terms are added and compared to the total column processes (shown on the right side of Fig. 10), it is clear that horizontal moisture advection is the largest contributor to the propagation of the precipitation anomalies.

When considering the processes that maintain the MJO-related precipitation anomalies, shown in the bottom panel of Fig. 10, it is clear that vertical moisture advection from longwave radiation and convective column processes C_c' act to maintain the rain area against the dissipative action of horizontal moisture advection and reduced surface latent heat fluxes. This result is consistent with previous studies on the moisture and moist static energy budget (Andersen and Kuang 2012; Chikira 2014; Wolding and Maloney 2015; Arnold et al. 2015), and consistent with Fig. 10 of Wolding et al. (2016), with the notable difference of C_c' contributing more significantly to the maintenance of the MJO. It is unclear if this difference is due to the method of analysis employed here or to a difference in physical processes that maintain the MJO in the two datasets.

From inspection of Figs. 5–9, it is clear that P' and $\partial P'/\partial t$ are not in quadrature. Rather, the two fields are shifted such that $\partial P'/\partial t$ is positive over the eastern side of the rain area 20°–60° to the east of the reference
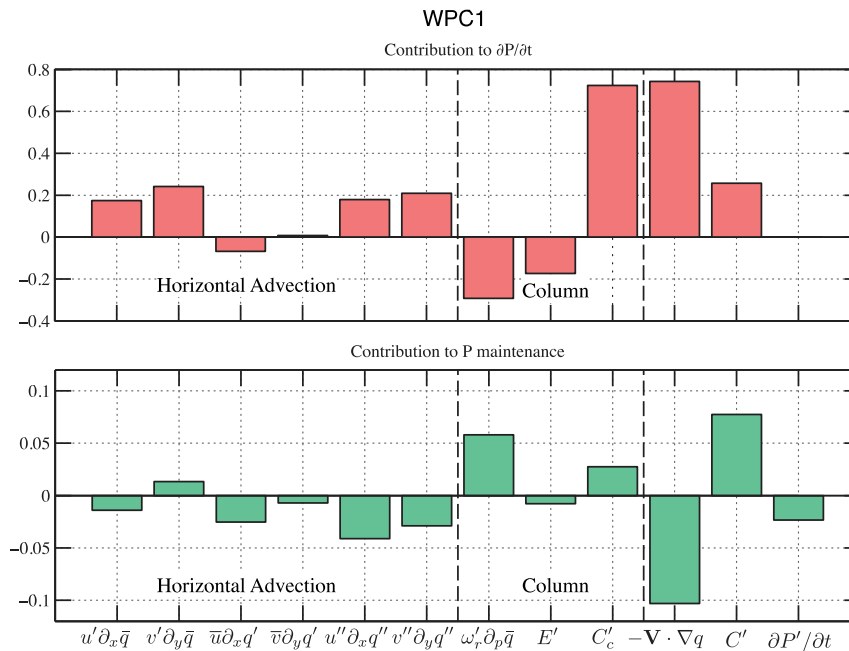
FIG. 10. Normalized contribution of the individual terms in the precipitation budget [Eq. (14)] to the (top) propagation and (bottom) maintenance of the precipitation anomalies for WPC1. The contributions are obtained by using Eq. (18b), projecting each term to the horizontal structure of column-integrated moisture tendency within 100° of the reference longitude and 15°N–15°S. The horizontal moisture advection term $-\mathbf{V}\cdot\nabla q$ corresponds to the contribution from the sum of all the horizontal advection terms, which are the first six terms, denoted as "horizontal advection." The column process term C' is the sum of the three terms denoted as "column."

longitude and negative near and to the west of the reference longitude. These regions are characterized by different vertical structures of humidity and vertical velocity (see Figs. 6–8 in AW3). Thus, different processes may maintain P' in the eastern and western sectors of the region of active convection. The contributions to the maintenance of P', separated into the eastern and western sectors is shown in Fig. 11, along with partially zonally averaged cross sections that further elucidates the structure of the relative humidity and circulation features in each sector. From 20°–60° to the east of the reference longitude (right panel), C'_c is the single dominant term that maintains the rain area, and $\partial P'/\partial t > 0$. Hence, the vertical velocity profile is shallower and is moistening the atmosphere. More complex dynamics dominate 20°–60° to the west of the reference longitude. Ascent driven by radiative heating and surface evaporation acts to maintain the rain area but is smaller in magnitude than the drying by horizontal moisture advection and C'_c, and $\partial P'/\partial t$ is negative as a result. The middle sector (within 20° of the reference longitude; middle panel) is a two-way balance between ascent driven by longwave radiative feedbacks and drying by horizontal advection from high-frequency eddy activity.

It is worth mentioning that nearly identical results to those in Fig. 10 were obtained for WPC2 (not shown), indicating that the same processes control the maintenance of the MJO throughout its life cycle.

We can similarly analyze variations in the processes responsible for MJO propagation, shown in Fig. 12. In contrast to the previous figure, which showed the region of anomalous precipitation, here we show WPC2, which shows, from east to west (from right to left), the transition from anomalously dry to anomalously moist conditions. In all three sectors a positive $\partial P'/\partial t$ is observed, indicating that the intraseasonal precipitation anomalies are increasing. Of all the moistening processes, C'_c is the only process that shows a positive value in all three sectors. Inspection of the individual cross sections reveals that, even though the profiles of vertical motion vary widely in these sectors, all three sectors are characterized by boundary layer convergence. In contrast, the left panel of Fig. 10 shows strong boundary layer divergence associated with negative C'_c. These patterns suggest that boundary layer processes play a central role in C'_c. While total horizontal advection plays an important role the propagation of the intraseasonal precipitation anomalies in all three

WPC1
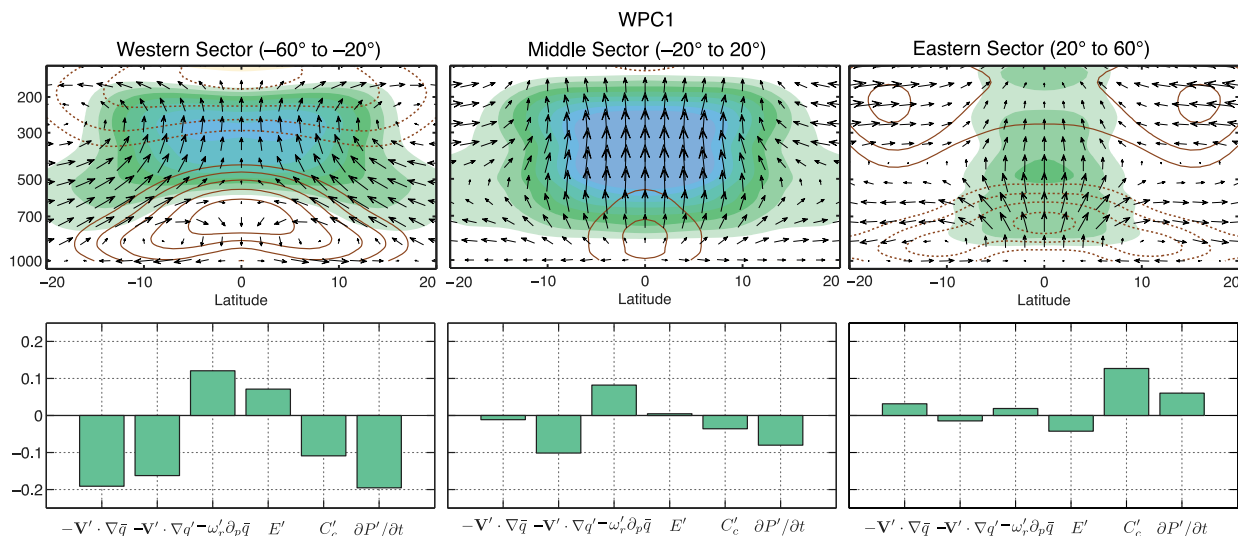
FIG. 11. (top) Composite meridional cross sections partially averaged in regions defined as (left) the western sector extending from 20° to 60° to the west of the reference longitude and (right) the eastern sector 20°–60° to the east of the reference longitude, as in Fig. 16 of AW3. Each cross section shows the meridional mass circulation (arrows) and the relative humidity anomaly (shading). The largest meridional flux vector is about $0.1 \, \mathrm{kg \, m^2 \, s^{-1}}$, and the largest vertical flux vector is about $4 \times 10^{-4} \, \mathrm{kg \, m^2 \, s^{-1}}$. (bottom) As in Fig. 10 (bottom), but separated into the western and eastern sectors.

sectors, there is an east-to-west (right to left) shift in the processes responsible for such advection. In the eastern sector, horizontal moisture advection is dominated by high-frequency eddy activity, transitioning to advection of low-frequency moisture by the MJO flow. By looking at the cross sections and inspecting Figs. 7 and 10, it is clear that the eddy contribution to horizontal moisture advection can be thought of as a diffusion of the elevated relative humidity anomalies, as it becomes a maximum near and to the west of the intraseasonal precipitation anomalies, hence projecting both onto the precipitation anomalies and the tendency. This is consistent with the findings of Peters et al. (2008) and Maloney et al. (2010), who found that high-frequency eddy activity acts to diffuse the intraseasonal moisture anomalies.

5. Summary and conclusions

In this study we derived a precipitation budget for the MJO that can adequately describe the propagation of the MJO-related precipitation anomalies across the Indo-Pacific warm pool (60°E–180°). This study is motivated by the increasing evidence that the anomalous circulation response to diabatic heating, in the form of precipitation, is central to the propagation of the MJO (Zhao et al. 2013; Pritchard and Bretherton 2014; Kim et al. 2014a; AW3; AWM; Adames and Kim 2016; Jiang 2017; among others). A precipitation estimate is obtained by scaling the ERA-Interim column water vapor

product to account for spatial variations in the sensitivity of precipitation to changes in tropospheric moisture (see Figs. 1–4). This sensitivity can be accounted for through the use of a spatially varying convective adjustment scale (Betts and Miller 1986; Bretherton et al. 2004). By using this time scale, a horizontal distribution of precipitation for the MJO is obtained that is largely in agreement with satellite-derived distributions of precipitation and agrees better with observations than the ERA-Interim precipitation product. The relationship between anomalous precipitation and column moisture presented here reveals three factors in addition to moisture that determine the amplitude of the MJO-related precipitation features:

- the amplitude of the low-frequency, climatological distribution of precipitation;
- the sensitivity of precipitation to changes in column relative humidity; and
- the column-integrated low-frequency, climatological saturation specific humidity.

All three of these terms are taken into account when defining the convective adjustment time scale $\overline{\tau_c}$. It was shown that intraseasonal rainfall variance is spatially correlated with $\overline{\nu_c} = \overline{\tau_c}^{-1}$. Because $\overline{\nu_c}$ is proportional to the climatological distribution of precipitation (which is, in turn, related to other variables such as the SST field), the derived precipitation field directly relates intraseasonal variability to the mean state. While it has been recognized by several previous studies that the aforementioned
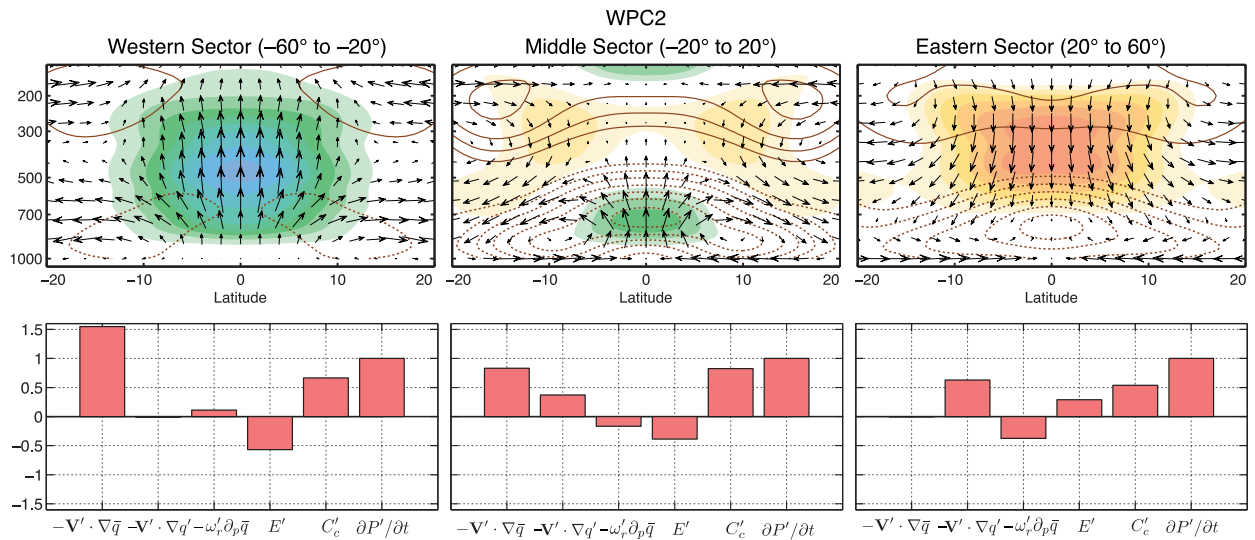
FIG. 12. As in Fig. 11, but for WPC2 and the bars depict the contribution to propagation of the precipitation anomalies. Note that for WPC2 the reference longitude corresponds to the node in $\Delta\chi$.

factors are important to MJO dynamics (Mapes and Bacmeister 2012; Kim et al. 2014b,c), they are shown here through a set of simple mathematical relations. These mathematical relations can be used to test MJO performance in GCM studies. For example, a recent study by Jiang et al. (2016) showed that the value of $\overline{\tau_c}$ is correlated with a model's ability to represent the MJO. Moreover, the climatological-mean rainfall and the saturation column water vapor, which define $\overline{\tau_c}$, are known to change in simulations that vary CO_2 concentrations (Allen and Ingram 2002; Held and Soden 2006; Seager et al. 2010). It may be of interest to study how $\overline{\tau_c}$ changes with climate change, as it may have implications for the MJO.

Using the aforementioned relationship, we can convert the column-integrated moisture budget into an intraseasonal precipitation budget. Using such a budget, under the assumption that weak temperature gradient balance is achieved, yields a concise description of the evolution of the intraseasonal precipitation anomalies throughout the MJO's life cycle.

It is found that the processes that moisten the near-equatorial region are more important for the maintenance and propagation of the intraseasonal precipitation anomalies than simple moisture and most static energy budget analyses suggest. This is a result of precipitation over the warm pool being more sensitive to moisture (smaller $\overline{\tau_c}$) in the near-equatorial warm pool (within 10°N–10°S). The near-equatorial moistening is dominated by the "convective column" process, which describes the net moistening by convectively driven vertical motion, condensation, rain reevaporation, and small-scale eddies. It is found that this moistening is

spatially correlated with ω_2, the profile of vertical motion that describes whether ascent is shallow or elevated. In regions where ascent is shallower (more bottom heavy), significant moistening occurs, while drying is observed in association with more elevated stratiform convection. Wolding et al. (2016) also found that C'_c (defined in their study as a net moistening by microphysics) moistens the free troposphere over a broad region to the east of the precipitation anomalies, and dries the atmosphere near and to the west of it, exhibiting a vertical profile that is qualitatively consistent with shallower vertical motion ω_2. These results are consistent with many previous studies (Benedict and Randall 2007; Del Genio et al. 2012; Lappen and Schumacher 2014; Johnson et al. 2015; Kim et al. 2015). While many studies have indicated that the profile of vertical motion is critical to the propagation of the MJO (Hannah et al. 2016; Janiga and Zhang 2016), it has been difficult to show in reanalysis data due to the influence of other processes such as radiative feedbacks. This adds to the body of evidence that highlights the importance of the sensitivity of convective parametrizations to moisture to the simulation of the MJO, as indicated by Derbyshire et al. (2004), Mapes and Bacmeister (2012), and Kim et al. (2014c), among others.

Near and to the west of the region where the anomalous precipitation is a maximum, horizontal moisture advection plays a key role in the damping and propagation of the precipitation anomalies. The dominant term is initially nonlinear advection by high-frequency eddies and transitions to advection of mean moisture by the MJO-related winds. The systematic evolution of

precipitation in the MJO, initially dominated by vertical advection followed by drying by horizontal advection, is remarkably similar to the life cycle of convectively coupled events described by Inoue and Back (2015) (see their Fig. 10) and is consistent with the simulations of Janiga and Zhang (2016).

In spite of the variety of processes described here that induced eastward propagation of the MJO, many of these processes can be attributed to the Matsuno–Gill response to an equatorial heat source. One of these wave-driven processes may be frictional moisture convergence (Wang and Rui 1990; Salby and Hendon 1994; Wang and Li 1994; Maloney and Hartmann 1998). It was shown in AW2 that the second baroclinic mode in vertical motion ω_2 is proportional to the difference between anomalous divergence in the free-tropospheric layer and in the boundary layer (their Fig. 12). It was further shown that the anomalous boundary layer divergence can be approximately represented as an MJO-driven equatorial Ekman pumping (their Fig. 11). Thus it seems likely that the convective column process C_c' described here is, at least, partially driven by frictional moisture convergence. It is important to note that convective feedbacks are likely equally important (Raymond and Herman 2012), and both processes may feed back on one another in ways that are difficult to quantify (Powell 2016). In addition to frictional convergence, horizontal moisture advection by the lower-tropospheric winds in the Matsuno–Gill response is also of central importance to the propagation of the rain area. The only important moistening process that is not clearly related to the anomalous MJO flow is moistening by high-frequency eddy activity. Because this contribution is confined near and to the west of the rainfall anomalies, this term may be an eddy diffusion process of the relative humidity anomalies, which exhibit a similar phasing relative to the anomalous precipitation.

It is also found that the processes that maintain the MJO-related anomalies are zonally varying with respect to the rain area. In the eastern region of precipitation, convective processes are the most important contributor to the maintenance of the anomalies and are also associated with increasing precipitation. Because precipitation is shallower in this region, it can be inferred that this "bottom heavy" precipitation is moistening the free troposphere ahead of the precipitation maximum, consistent with the notion of a negative "gross moist stability" (Neelin and Held 1987; Raymond et al. 2009). During the later stages of the active phase, precipitation is predominantly maintained by longwave radiative feedbacks, augmented by enhanced surface latent heat fluxes, consistent with the results from previous studies (Andersen and Kuang 2012; Kim et al.

2014a; Sobel et al. 2014; Wolding and Maloney 2015; Arnold et al. 2015; among others). This result suggests that, as Del Genio et al. (2015) pointed out, both the interactions between moisture and convection, and between convection and radiation, need to be adequately represented in order to successfully simulate an MJO.

The framework presented here can be directly compared to the so-called moisture-mode theoretical framework of the MJO and related frameworks that use simplified Betts–Miller schemes in their representation of precipitation (Wang and Chen 2016; Wang et al. 2016). It can also be extended to other theories of the MJO where the precipitation field is parameterized as a function of a low-frequency variable, such as in the work of Yang and Ingersoll (2013, 2014). For example, in AK16 a constant value for $\overline{\tau_c}$ was used, among other approximations, to obtain linear solutions to the precipitation budget [Eq. (14)]. A spatially varying $\overline{\tau_c}$ will affect the propagation of the MJO by confining the anomalies to regions where $\overline{\tau_c}$ is small (large $\overline{\nu_c}$). The intraseasonal precipitation anomalies will weaken as they propagate eastward toward the equatorial central Pacific, a region where the convective time scale is large ($\overline{\nu_c} \to 0$, see Fig. 2d). Also, by generalizing the framework of AK16, we can also expect that wave energy will weaken as it propagates westward into the African continent, where $\overline{\nu_c} \to 0$. Thus, in this framework, the convective anomalies of the MJO are bounded to the Indo-Pacific warm pool, where rainfall is most sensitive to moisture. In observations, the circulation anomalies decouple from the anomalous convection and sometimes recouple over the eastern Pacific or again over the Indian Ocean (Maloney and Esbensen 2003, 2007; Haertel et al. 2015). For this recoupling to be taken into account, other processes like changes in the buoyancy of free troposphere need to be taken into account (Powell 2016).

There are a few caveats to this study. For once, a significant residual exists in the ERA-Interim moisture budget, which represents a missing moisture source or an excessive moisture sink in the product. We have assumed that this residual in the moisture budget is due to an inadequate representation of convection in the reanalysis, as was suggested by Mapes and Bacmeister (2012) for MERRA. Thus, we have included this residual as a part of the so-called convective column process, since it most likely affects this term, following previous work (AW3; Wolding and Maloney 2015). A more complete study can be made by also analyzing models that simulate strong MJOs. Furthermore, we also assumed that longwave radiative heating projects onto the first baroclinic mode in
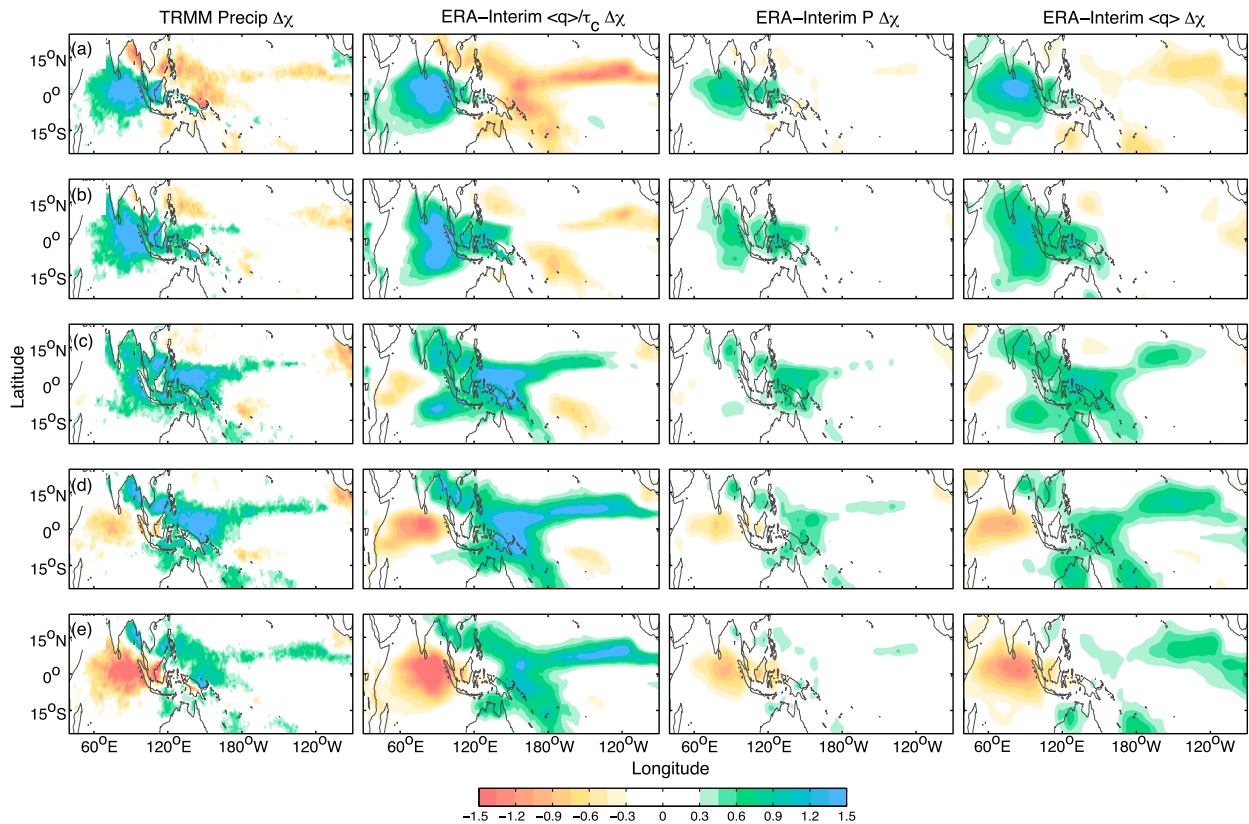
FIG. A1. Five-panel sequence of (left) TRMM 3B42 precipitation, (center left) precipitation estimated from the equation $\langle q' \rangle / \overline{\tau_c}$, (center right) ERA-Interim precipitation, and (right) ERA-Interim column water vapor $\langle q' \rangle$, regressed on linear combinations of PC1 and PC2 of $\Delta \chi$: (a) $-$PC2, (b) (PC1 $-$ PC2)$/\sqrt{2}$, (c) PC1, (d) (PC1 $-$ PC2)$/\sqrt{2}$, and (e) PC2. The linear combinations roughly correspond to phases 3–7 in the Wheeler and Hendon (2004) multivariate index. Shading is in units of mm day^{-1} for (left)–(center right) and in units of mm for (right).

vertical motion, which may introduce errors into the analysis presented here. In spite of these caveats, the consistency of the patterns presented here attests to the robustness of the results.

While a substantial amount of insight is obtained from using a precipitation budget, the loss of vertically resolved processes may be a limitation to the interpretation of the results from this study. For example, it was shown by Chikira (2014) and Wolding and Maloney (2015) that shortwave radiative heating exhibits a vertical dipole that is approximately canceled out when vertically integrated. Since precipitation is closely related to vertical motion, which is highly correlated in space with the vertically resolved relative humidity (see Figs. 3 and 10 in AW3), it may be possible to use relative humidity in order to obtain an equation for vertically resolved diabatic heating.

Finally, it is worth mentioning that moisture in itself is not a cause of precipitation; rather, it is correlated to the amount of precipitation that occurs over given region. As discussed by Raymond et al. (2015) and references

therein, precipitation is often the result of changes in the thermodynamic profile of the atmosphere, such as modulation of convective available potential energy (CAPE) or convective inhibition (CIN). It can also result when changes in the atmospheric circulation modulate vertical motion in a given region. A more comprehensive understanding of the propagation of the rain area in the MJO requires further understanding of the cause of precipitation in the MJO cycle.

APPENDIX

Regression Maps of Moisture and Precipitation

Figure A1 shows five-panel sequences of MJO-related precipitation anomalies from TRMM 3B42, the estimated precipitation $P' = \langle q' \rangle / \overline{\tau_c}$, and ERA-Interim precipitation compared to column water vapor $\langle q' \rangle$. While ERA-Interim precipitation is spatially consistent with TRMM's distribution of precipitation, its magnitude is approximately half as large (see also Fig. 1 in AW3). Although the resolution is coarser, the estimated precipitation P' exhibits a similar magnitude and spatial distribution to TRMM over the points in the warm pool that are occurring over the ocean. The estimated precipitation is too high compared to TRMM over the Pacific ITCZ and over the landmasses of the Maritime Continent. In comparison, the column moisture anomalies are broader in scale and do not always correspond spatially with precipitation anomalies, as seen near the eastern Pacific coast in Figs. A1a and A1e and Australia in Figs. A1c and A1d.

REFERENCES

Adames, Á. F., and J. M. Wallace, 2014a: Three-dimensional structure and evolution of the MJO and its relation to the mean flow. *J. Atmos. Sci.*, **71**, 2007–2026, doi:10.1175/JAS-D-13-0254.1.

——, and ——, 2014b: Three-dimensional structure and evolution of the vertical velocity and divergence fields in the MJO. *J. Atmos. Sci.*, **71**, 4661–4681, doi:10.1175/JAS-D-14-0091.1.

——, and ——, 2015: Three-dimensional structure and evolution of the moisture field in the MJO. *J. Atmos. Sci.*, **72**, 3733–3754, doi:10.1175/JAS-D-15-0003.1.

——, and D. Kim, 2016: The MJO as a dispersive, convectively coupled moisture wave: Theory and observations. *J. Atmos. Sci.*, **73**, 913–941, doi:10.1175/JAS-D-15-0170.1.

——, J. M. Wallace, and J. M. Monteiro, 2016: Seasonality of the structure and propagation characteristics of the MJO. *J. Atmos. Sci.*, **73**, 3511–3526, doi:10.1175/JAS-D-15-0232.1.

Ahmed, F., and C. Schumacher, 2015: Convective and stratiform components of the precipitation-moisture relationship. *Geophys. Res. Lett.*, **42**, 10 453–10 462, doi:10.1002/2015GL066957.

Allen, M. R., and W. J. Ingram, 2002: Constraints on future changes in climate and the hydrologic cycle. *Nature*, **419**, 224–232, doi:10.1038/nature01092.

Andersen, J. A., and Z. Kuang, 2012: Moist static energy budget of MJO-like disturbances in the atmosphere of a zonally symmetric aquaplanet. *J. Climate*, **25**, 2782–2804, doi:10.1175/JCLI-D-11-00168.1.

Arnold, N. P., Z. Kuang, and E. Tziperman, 2013: Enhanced MJO-like variability at high SST. *J. Climate*, **26**, 988–1001, doi:10.1175/JCLI-D-12-00272.1.

——, M. Branson, Z. Kuang, D. A. Randall, and E. Tziperman, 2015: MJO intensification with warming in the superparameterized CESM. *J. Climate*, **28**, 2706–2724, doi:10.1175/JCLI-D-14-00494.1.

Benedict, J. J., and D. A. Randall, 2007: Observed characteristics of the MJO relative to maximum rainfall. *J. Atmos. Sci.*, **64**, 2332–2354, doi:10.1175/JAS3968.1.

Betts, A. K., 1986: A new convective adjustment scheme. Part I: Observational and theoretical basis. *Quart. J. Roy. Meteor. Soc.*, **112**, 677–691, doi:10.1002/qj.49711247307.

——, and M. J. Miller, 1986: A new convective adjustment scheme. Part II: Single column tests using GATE wave, BOMEX, ATEX and arctic air-mass data sets. *Quart. J. Roy. Meteor. Soc.*, **112**, 693–709, doi:10.1002/qj.49711247308.

Birch, C. E., S. Webster, S. C. Peatman, D. J. Parker, A. J. Matthews, Y. Li, and M. E. E. Hassim, 2016: Scale interactions between the MJO and the western Maritime Continent. *J. Climate*, **29**, 2471–2492, doi:10.1175/JCLI-D-15-0557.1.

Bretherton, C. S., and P. K. Smolarkiewicz, 1989: Gravity waves, compensating subsidence and detrainment around cumulus clouds. *J. Atmos. Sci.*, **46**, 740–759, doi:10.1175/1520-0469(1989)046<0740:GWCSAD>2.0.CO;2.

——, M. E. Peters, and L. E. Back, 2004: Relationships between water vapor path and precipitation over the tropical oceans. *J. Climate*, **17**, 1517–1528, doi:10.1175/1520-0442(2004)017<1517:RBWVPA>2.0.CO;2.

Charney, J. G., 1963: A note on large-scale motions in the tropics. *J. Atmos. Sci.*, **20**, 607–609, doi:10.1175/1520-0469(1963)020<0607:ANOLSM>2.0.CO;2.

Chikira, M., 2014: Eastward-propagating intraseasonal oscillation represented by Chikira–Sugiyama cumulus parameterization. Part II: Understanding moisture variation under weak temperature gradient balance. *J. Atmos. Sci.*, **71**, 615–639, doi:10.1175/JAS-D-13-038.1.

Dee, D. P., and Coauthors, 2011: The ERA-Interim reanalysis: Configuration and performance of the data assimilation system. *Quart. J. Roy. Meteor. Soc.*, **137**, 553–597, doi:10.1002/qj.828.

Del Genio, A. D., Y. Chen, D. Kim, and M.-S. Yao, 2012: The MJO transition from shallow to deep convection in *CloudSat*/CALIPSO data and GISS GCM simulations. *J. Climate*, **25**, 3755–3770, doi:10.1175/JCLI-D-11-00384.1.

——, J. Wu, A. B. Wolf, Y. Chen, M.-S. Yao, and D. Kim, 2015: Constraints on cumulus parameterization from simulations of observed MJO events. *J. Climate*, **28**, 6419–6442, doi:10.1175/JCLI-D-14-00832.1.

Derbyshire, S. H., I. Beau, P. Bechtold, J.-Y. Grandpeix, J.-M. Piriou, J.-L. Redelsperger, and P. M. M. Soares, 2004: Sensitivity of moist convection to environmental humidity. *Quart. J. Roy. Meteor. Soc.*, **130**, 3055–3079, doi:10.1256/qj.03.130.

Duchon, C. E., 1979: Lanczos filtering in one and two dimensions. *J. Appl. Meteor.*, **18**, 1016–1022, doi:10.1175/1520-0450(1979)018<1016:LFIOAT>2.0.CO;2.

Frierson, D. M. W., 2007: The dynamics of idealized convection schemes and their effect on the zonally averaged tropical circulation. *J. Atmos. Sci.*, **64**, 1959–1976, doi:10.1175/JAS3935.1.

Gill, A. E., 1980: Some simple solutions for heat-induced tropical circulation. *Quart. J. Roy. Meteor. Soc.*, **106**, 447–462, doi:10.1002/qj.49710644905.

Haertel, P., K. Straub, and A. Budsock, 2015: Transforming circumnavigating Kelvin waves that initiate and dissipate the Madden–Julian Oscillation. *Quart. J. Roy. Meteor. Soc.*, **141**, 1586–1602, doi:10.1002/qj.2461.

Hannah, W. M., B. E. Mapes, and G. S. Elsaesser, 2016: A Lagrangian view of moisture dynamics during DYNAMO. *J. Atmos. Sci.*, **73**, 1967–1985, doi:10.1175/JAS-D-15-0243.1.

Held, I. M., and B. J. Soden, 2006: Robust responses of the hy-
drological cycle to global warming. *J. Climate*, **19**, 5686–5699,
doi:10.1175/JCLI3990.1.

Holloway, C. E., and J. D. Neelin, 2009: Moisture vertical structure,
column water vapor, and tropical deep convection. *J. Atmos.
Sci.*, **66**, 1665–1683, doi:10.1175/2008JAS2806.1.

Houze, R. A., Jr., 1982: Cloud clusters and large-scale vertical
motions in the tropics. *J. Meteor. Soc. Japan*, **60**, 396–410,
doi:10.2151/jmsj1965.60.1_396.

Hsu, P.-c., and T. Li, 2012: Role of the boundary layer moisture
asymmetry in causing the eastward propagation of the
Madden-Julian oscillation. *J. Climate*, **25**, 4914–4931,
doi:10.1175/JCLI-D-11-00310.1.

Huffman, G. J., and Coauthors, 2007: The TRMM Multisatellite
Precipitation Analysis (TMPA): Quasi-global, multiyear,
combined-sensor precipitation estimates at fine scales.
J. Hydrometeor., **8**, 38–55, doi:10.1175/JHM560.1.

Inoue, K., and L. E. Back, 2015: Gross moist stability assessment
during TOGA COARE: Various interpretations of gross
moist stability. *J. Atmos. Sci.*, **72**, 4148–4166, doi:10.1175/
JAS-D-15-0092.1.

Janiga, M. A., and C. Zhang, 2016: MJO moisture budget during
DYNAMO in a cloud-resolving model. *J. Atmos. Sci.*, **73**,
2257–2278, doi:10.1175/JAS-D-14-0379.1.

Jiang, X., 2017: Key processes for the eastward propagation of
the Madden-Julian Oscillation based on multimodel simula-
tions. *J. Geophys. Res. Atmos.*, **122**, 755–770, doi:10.1002/
2016JD025955.

——, M. Zhao, E. D. Maloney, and D. E. Waliser, 2016: Convective
moisture adjustment time scale as a key factor in regulating
model amplitude of the Madden-Julian Oscillation. *Geophys.
Res. Lett.*, **43**, 10 412–10 419, doi:10.1002/2016GL070898.

Johnson, R. H., P. E. Ciesielski, J. H. Ruppert, and M. Katsumata,
2015: Sounding-based thermodynamic budgets for DYNAMO.
J. Atmos. Sci., **72**, 598–622, doi:10.1175/JAS-D-14-0202.1.

Kim, D., J.-S. Kug, and A. H. Sobel, 2014a: Propagating versus
nonpropagating Madden–Julian oscillation events. *J. Climate*,
27, 111–125, doi:10.1175/JCLI-D-13-00084.1.

——, M.-I. Lee, D. Kim, S. Schubert, D. Waliser, and B. Tian,
2014b: Representation of tropical subseasonal variability of
precipitation in global reanalyses. *Climate Dyn.*, **43**, 517–534,
doi:10.1007/s00382-013-1890-x.

——, and Coauthors, 2014c: Process-oriented MJO simulation di-
agnostic: Moisture sensitivity of simulated convection.
J. Climate, **27**, 5379–5395, doi:10.1175/JCLI-D-13-00497.1.

——, M.-S. Ahn, I.-S. Kang, and A. D. Del Genio, 2015: Role of
longwave cloud–radiation feedback in the simulation of the
Madden–Julian oscillation. *J. Climate*, **28**, 6979–6994,
doi:10.1175/JCLI-D-14-00767.1.

Kiranmayi, L., and E. D. Maloney, 2011: Intraseasonal moist static
energy budget in reanalysis data. *J. Geophys. Res.*, **116**,
D21117, doi:10.1029/2011JD016031.

Lappen, C.-L., and C. Schumacher, 2014: The role of tilted heating
in the evolution of the MJO. *J. Geophys. Res. Atmos.*, **119**,
2966–2989, doi:10.1002/2013JD020638.

Lau, W. K.-M., and D. E. Waliser, 2011: *Intraseasonal Variability in
the Atmosphere-Ocean Climate System*. Springer, 437 pp.,
doi:10.1007/b138817.

Liu, F., and B. Wang, 2016: Effects of moisture feedback in a
frictional coupled Kelvin–Rossby wave model and implication
in the Madden–Julian oscillation dynamics. *Climate Dyn.*, **48**,
513–522, doi:10.1007/s00382-016-3090-y.

Madden, R. A., and P. R. Julian, 1971: Detection of a 40–50 day
oscillation in the zonal wind in the tropical Pacific. *J. Atmos.
Sci.*, **28**, 702–708, doi:10.1175/1520-0469(1971)028<0702:
DOADOI>2.0.CO;2.

——, and ——, 1972: Description of global-scale circulation
cells in the tropics with a 40–50 day period. *J. Atmos. Sci.*,
29, 1109–1123, doi:10.1175/1520-0469(1972)029<1109:
DOGSCC>2.0.CO;2.

Maloney, E. D., 2009: The moist static energy budget of a com-
posite tropical intraseasonal oscillation in a climate model.
J. Climate, **22**, 711–729, doi:10.1175/2008JCLI2542.1.

——, and D. L. Hartmann, 1998: Frictional moisture convergence
in a composite life cycle of the Madden–Julian oscillation. *J.
Climate*, **11**, 2387–2403, doi:10.1175/1520-0442(1998)011<2387:
FMCIAC>2.0.CO;2.

——, and S. K. Esbensen, 2003: The amplification of east Pacific
Madden–Julian oscillation convection and wind anomalies
during June–November. *J. Climate*, **16**, 3482–3497, doi:10.1175/
1520-0442(2003)016<3482:TAOEPM>2.0.CO;2.

——, and ——, 2007: Satellite and buoy observations of bo-
real summer intraseasonal variability in the tropical
northeast Pacific. *Mon. Wea. Rev.*, **135**, 3–19, doi:10.1175/
MWR3271.1.

——, A. H. Sobel, and W. M. Hannah, 2010: Intraseasonal vari-
ability in an aquaplanet general circulation model. *J. Adv.
Model. Earth Syst.*, **2** (5), doi:10.3894/JAMES.2010.2.5.

Mapes, B. E., and J. T. Bacmeister, 2012: Diagnosis of tropical
biases and the MJO from patterns in the MERRA analysis
tendency fields. *J. Climate*, **25**, 6202–6214, doi:10.1175/
JCLI-D-11-00424.1.

Masunaga, H., 2012: Short-term versus climatological relationship
between precipitation and tropospheric humidity. *J. Climate*,
25, 7983–7990, doi:10.1175/JCLI-D-12-00037.1.

Matsuno, T., 1966: Quasi-geostrophic motions in the equatorial
area. *J. Meteor. Soc. Japan*, **44**, 25–43.

Neelin, J. D., and I. M. Held, 1987: Modeling tropical conver-
gence based on the moist static energy budget. *Mon. Wea.
Rev.*, **115**, 3–12, doi:10.1175/1520-0493(1987)115<0003:
MTCBOT>2.0.CO;2.

——, and N. Zeng, 2000: A quasi-equilibrium tropical circulation
model—Formulation. *J. Atmos. Sci.*, **57**, 1741–1766, doi:10.1175/
1520-0469(2000)057<1741:AQETCM>2.0.CO;2.

Peatman, S. C., A. J. Matthews, and D. P. Stevens, 2014: Propa-
gation of the Madden–Julian Oscillation through the Maritime
Continent and scale interaction with the diurnal cycle of pre-
cipitation. *Quart. J. Roy. Meteor. Soc.*, **140**, 814–825,
doi:10.1002/qj.2161.

Peters, M. E., Z. Kuang, and C. C. Walker, 2008: Analysis of at-
mospheric energy transport in ERA-40 and implications for
simple models of the mean tropical circulation. *J. Climate*, **21**,
5229–5241, doi:10.1175/2008JCLI2073.1.

Peters, O., and J. D. Neelin, 2006: Critical phenomena in atmo-
spheric precipitation. *Nat. Phys.*, **2**, 393–396, doi:10.1038/
nphys314.

Powell, S. W., 2016: Updraft buoyancy within and moistening by
cumulonimbi prior to MJO convective onset in a regional
model. *J. Atmos. Sci.*, **73**, 2913–2934, doi:10.1175/
JAS-D-15-0326.1.

——, and R. A. Houze Jr., 2015: Effect of dry large-scale vertical
motions on initial MJO convective onset. *J. Geophys. Res.
Atmos.*, **120**, 4783–4805, doi:10.1002/2014JD022961.

Pritchard, M. S., and C. S. Bretherton, 2014: Causal evidence that ro-
tational moisture advection is critical to the superparameterized

Madden–Julian oscillation. *J. Atmos. Sci.*, **71**, 800–815, doi:10.1175/JAS-D-13-0119.1.

Raymond, D. J., 2000: The Hadley circulation as a radiative–convective instability. *J. Atmos. Sci.*, **57**, 1286–1297, doi:10.1175/1520-0469(2000)057<1286:THCAAR>2.0.CO;2.

——, 2001: A new model of the Madden–Julian oscillation. *J. Atmos. Sci.*, **58**, 2807–2819, doi:10.1175/1520-0469(2001)058<2807:ANMOTM>2.0.CO;2.

——, and Ž. Fuchs, 2009: Moisture modes and the Madden–Julian oscillation. *J. Climate*, **22**, 3031–3046, doi:10.1175/2008JCLI2739.1.

——, and M. J. Herman, 2012: Frictional convergence, atmospheric convection, and causality. *Atmósfera*, **25**, 253–267.

——, S. L. Sessions, A. H. Sobel, and Ž. Fuchs, 2009: The mechanics of gross moist stability. *J. Adv. Model. Earth Syst.*, **1** (9), doi:10.3894/JAMES.2009.1.9.

——, Ž. Fuchs, S. Gjorgjievska, and S. Sessions, 2015: Balanced dynamics and convection in the tropical troposphere. *J. Adv. Model. Earth Syst.*, **7**, 1093–1116, doi:10.1002/2015MS000467.

Salby, M. L., and H. H. Hendon, 1994: Intraseasonal behavior of clouds, temperature, and motion in the tropics. *J. Atmos. Sci.*, **51**, 2207–2224, doi:10.1175/1520-0469(1994)051<2207:IBOCTA>2.0.CO;2.

Schumacher, C., R. A. Houze, and I. Kraucunas, 2004: The tropical dynamical response to latent heating estimates derived from the TRMM precipitation radar. *J. Atmos. Sci.*, **61**, 1341–1358, doi:10.1175/1520-0469(2004)061<1341:TTDRTL>2.0.CO;2.

Seager, R., N. Naik, and G. A. Vecchi, 2010: Thermodynamic and dynamic mechanisms for large-scale changes in the hydrological cycle in response to global warming. *J. Climate*, **23**, 4651–4668, doi:10.1175/2010JCLI3655.1.

Sobel, A. H., and C. S. Bretherton, 2000: Modeling tropical precipitation in a single column. *J. Climate*, **13**, 4378–4392, doi:10.1175/1520-0442(2000)013<4378:MTPIAS>2.0.CO;2.

——, and E. Maloney, 2012: An idealized semi-empirical framework for modeling the Madden–Julian oscillation. *J. Atmos. Sci.*, **69**, 1691–1705, doi:10.1175/JAS-D-11-0118.1.

——, and ——, 2013: Moisture modes and the eastward propagation of the MJO. *J. Atmos. Sci.*, **70**, 187–192, doi:10.1175/JAS-D-12-0189.1.

——, J. Nilsson, and L. M. Polvani, 2001: The weak temperature gradient approximation and balanced tropical moisture waves. *J. Atmos. Sci.*, **58**, 3650–3665, doi:10.1175/1520-0469(2001)058<3650:TWTGAA>2.0.CO;2.

——, S. Wang, and D. Kim, 2014: Moist static energy budget of the MJO during DYNAMO. *J. Atmos. Sci.*, **71**, 4276–4291, doi:10.1175/JAS-D-14-0052.1.

Sugiyama, M., 2009: The moisture mode in the quasi-equilibrium tropical circulation model. Part I: Analysis based on the weak temperature gradient approximation. *J. Atmos. Sci.*, **66**, 1507–1523, doi:10.1175/2008JAS2690.1.

Waliser, D., and Coauthors, 2009: MJO simulation diagnostics. *J. Climate*, **22**, 3006–3030, doi:10.1175/2008JCLI2731.1.

Wang, B., 1988: Dynamics of tropical low-frequency waves: An analysis of the moist Kelvin wave. *J. Atmos. Sci.*, **45**, 2051–2065, doi:10.1175/1520-0469(1988)045<2051:DOTLFW>2.0.CO;2.

——, and H. Rui, 1990: Dynamics of the coupled moist Kelvin–Rossby wave on an equatorial β-plane. *J. Atmos. Sci.*, **47**, 397–413, doi:10.1175/1520-0469(1990)047<0397:DOTCMK>2.0.CO;2.

——, and T. Li, 1994: Convective interaction with boundary-layer dynamics in the development of a tropical intraseasonal system. *J. Atmos. Sci.*, **51**, 1386–1400, doi:10.1175/1520-0469(1994)051<1386:CIWBLD>2.0.CO;2.

——, and G. Chen, 2016: A general theoretical framework for understanding essential dynamics of Madden–Julian oscillation. *Climate Dyn.*, 1–20, doi:10.1007/s00382-016-3448-1.

——, F. Liu, and G. Chen, 2016: A trio-interaction theory for Madden–Julian oscillation. *Geosci. Lett.*, **3**, 34, doi:10.1186/s40562-016-0066-z.

Wheeler, M. C., and H. H. Hendon, 2004: An all-season real-time multivariate MJO index: Development of an index for monitoring and prediction. *Mon. Wea. Rev.*, **132**, 1917–1932, doi:10.1175/1520-0493(2004)132<1917:AARMMI>2.0.CO;2.

Wolding, B. O., and E. D. Maloney, 2015: Objective diagnostics and the Madden–Julian oscillation. Part II: Application to moist static energy and moisture budgets. *J. Climate*, **28**, 7786–7808, doi:10.1175/JCLI-D-14-00689.1.

——, ——, and M. Branson, 2016: Vertically resolved weak temperature gradient analysis of the Madden-Julian Oscillation in SP-CESM. *J. Adv. Model. Earth Syst.*, **8**, 1586–1619, doi:10.1002/2016MS000724.

Yang, D., and A. P. Ingersoll, 2013: Triggered convection, gravity waves, and the MJO: A shallow-water model. *J. Atmos. Sci.*, **70**, 2476–2486, doi:10.1175/JAS-D-12-0255.1.

——, and ——, 2014: A theory of the MJO horizontal scale. *Geophys. Res. Lett.*, **41**, 1059–1064, doi:10.1002/2013GL058542.

Yasunaga, K., and B. Mapes, 2012: Differences between more divergent and more rotational types of convectively coupled equatorial waves. Part I: Space–time spectral analyses. *J. Atmos. Sci.*, **69**, 3–16, doi:10.1175/JAS-D-11-033.1.

Yoneyama, K., C. Zhang, and C. N. Long, 2013: Tracking pulses of the Madden–Julian oscillation. *Bull. Amer. Meteor. Soc.*, **94**, 1871–1891, doi:10.1175/BAMS-D-12-00157.1.

Zhang, C., 2005: Madden-Julian Oscillation. *Rev. Geophys.*, **43**, RG2003, doi:10.1029/2004RG000158.

——, 2013: Madden–Julian oscillation: Bridging weather and climate. *Bull. Amer. Meteor. Soc.*, **94**, 1849–1870, doi:10.1175/BAMS-D-12-00026.1.

——, and J. Ling, 2012: Potential vorticity of the Madden–Julian oscillation. *J. Atmos. Sci.*, **69**, 65–78, doi:10.1175/JAS-D-11-081.1.

——, J. Gottschalck, E. D. Maloney, M. W. Moncrieff, F. Vitart, D. E. Waliser, B. Wang, and M. C. Wheeler, 2013: Cracking the MJO nut. *Geophys. Res. Lett.*, **40**, 1223–1230, doi:10.1002/grl.50244.

Zhao, C., T. Li, and T. Zhou, 2013: Precursor signals and processes associated with MJO initiation over the tropical Indian Ocean. *J. Climate*, **26**, 291–307, doi:10.1175/JCLI-D-12-00113.1.

Zhu, H., and H. Hendon, 2015: Role of large scale moisture advection for simulation of the MJO with increased entrainment. *Quart. J. Roy. Meteor. Soc.*, **141**, 2127–2136, doi:10.1002/qj.2510.